# Semiconductor superlattices in optoelectronic devices

## Part II: Device structures and characteristics

M. A. HERMAN

Institute of Vacuum Technology
ul. Długa 44/50, 00-241 Warszawa,
and Institute of Physics, Polish Academy of Sciences,
al. Lotników 32/46, 02-668, Warszawa, Poland

## 1. Introduction

Quantum wells separated by potential barrier layers are the basic structural elements of superlattices (SL). Sometimes, the thickness of the barrier layers is larger than the extension of electron and hole wave functions in the barrier semiconductor. In such a case the charge carriers are confined to individual quantum wells of the SL structure, thus, they cannot penetrate throughout the barriers into the neighboring wells. No tunneling, and consequently, no coupling between the quantum wells occurs in this case. The carriers in the quantum wells may be treated as two-dimensional electron or hole gas (2DEG, 2DHG), whereas the whole layer structure has to be called a multi quantum well (MQW) structure. This structure rather exhibits properties of a single quantum well in multiplication than properties typical of a SL structure. Therefore, MQW structures should not be considered as superlattices.

In a real SL structure the carrier wave functions penetrate throughout the potential barriers. Consequently, the charge carriers behave there as three-dimensional electron or hole gas (3DEG, 3DHG).

MQW structures have found wide application in device structures. High mobility transistors, quantum well lasers, and quantum well photodetectors may serve here as examples [1]. However, in this paper only the device application of SL structures will be considered.

The characteristic feature of optoelectronics is that, instead of the electronic channel used in conventional electronics, it makes use of an optical channel for data transmission and processing. The basic semiconductor elements of an optical data transmission channel are: an electrically controlled source of electromagnetic radiation (i.e., light emitting diode or junction laser), an element which processes or transmits optical signals (e.g., waveguide, modulator, deflector, directional coupler, etc.), and an element which converts light into electric signals (photodetector). So far, SL structures have been applied mainly in light sources and in photodetectors. Therefore, only such application of these structures will be considered in this paper.

Many interesting application possibilities of SL structures in semiconductor light sources and photodetectors have been demonstrated in the last few years [2]. The operating principles of these devices include at least one of the following concepts, namely: (i) spatial confinement of charge carriers and light, (ii) spatial separation of electrons from holes or free carriers from their parent impurities, (iii) rapid transfer of charge carriers across the boundary between thin heterolayers of the device structure, with a simultaneous increase in kinetic energy of carriers, and others. Usually, all of these concepts can be done more effectively if SLs are used as construction elements in the structures of the considered optoelectronic devices. The intention of the paper is to convince the Reader that this statement is true.

## 2. Light emitting diodes

In semiconductor light sources emitting incoherent light, namely, in light emitting diodes (LED), superlattices are used in order to: (i) gain an extraordinarily large stability of the luminescence peak energy at high excitation intensities, (ii) obtain generation of light from III–V compounds in the far infrared region, (iii) intensify the emission of blue light sources, and (iv) get sources emitting light of anizotropic polarization. The applications listed above are illustrated by the examples of devices presented in this Section.

### 2.1. Sawtooth superlattice LED

The doping concentration and real-space energy band diagram of the edge-emitting sawtooth superlattice LED [3÷5] is shown in Fig. 1. The structure (Fig. 2) is grown by molecular

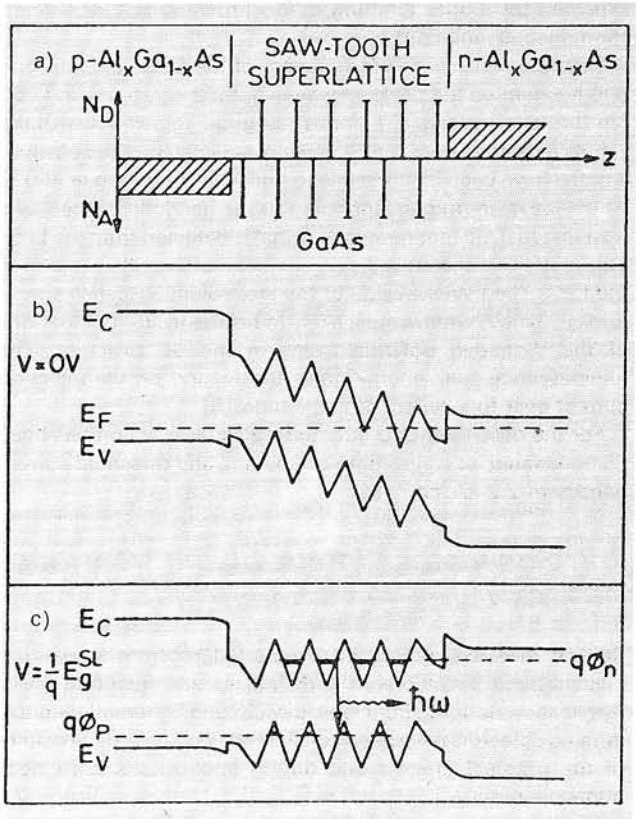


Fig. 1. Doping concentration and real-space energy band diagram of the sawtooth SL LED (not to scale): a) Real-space distribution of dopants concentration in the confinement AlGaAs layers and in the SL structure of the diode active layer, b) Sawtooth shaped band diagram of the active layer and the adjacent confinement layers at zero bias, c) at a forward bias of $V \approx E_g^{SL}/q = \varphi_n - \varphi_p$ (from Ref. [5])

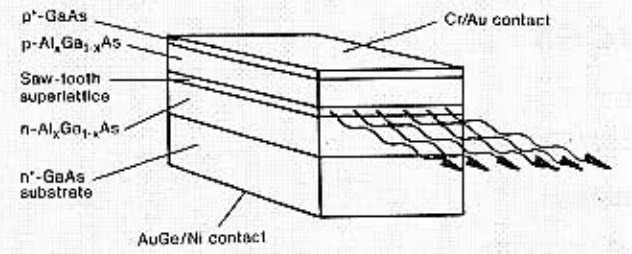


Fig. 2. Layer sequence in the device structure of the sawtooth SL LED (from Ref. [2])

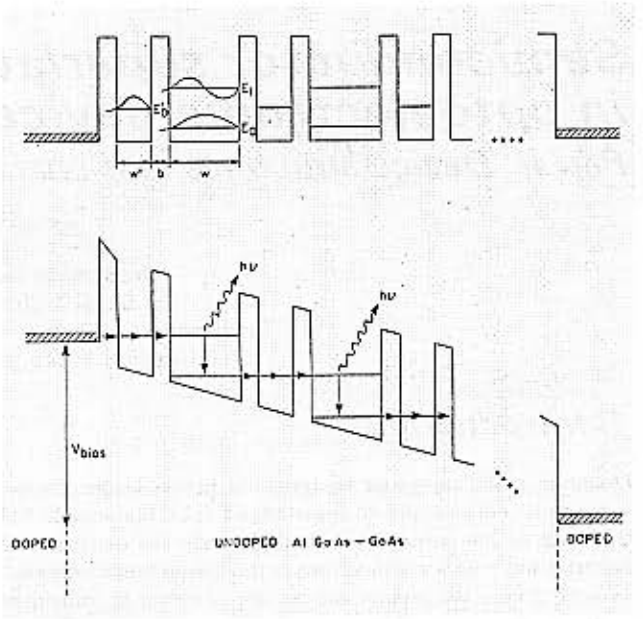


Fig. 3. Conduction-band edge profile of the far IR LED under zero bias (upper part), and the biased device in operation (lower part). Heavily doped contact layers at the ends of the structure are hatched to show the positions of the Fermi levels there. IR light emission occurs in the wide wells (from Ref. [7])

beam epitaxy (MBE) on heavily doped $n^+$-GaAs substrate (see part I of this paper [6]). The epitaxially grown layers are $n$- and $p$-type $Al_xGa_{1-x}As$, for optical confinement of the sawtooth SL region. The top $p^+$-GaAs layer facilitates ohmic contact formation.

The superlattice bandgap energy is stable in this LED structure even at high excitation intensities. This stability is very useful from the point of view of operation characteristics of the considered LED. The integrated electroluminescence intensity of the LED depends linearly on the injection current, as expected for diodes emitting monochromatic but incoherent spontaneous radiation.

Electroluminescence (EL) spectra of the LEDs operating at 300 K exhibited the peaks at wavelengths $\lambda = 925$ nm and 965 nm (for two investigated diodes), in good agreement with the values expected from the SL design parameters. These wavelengths have been inaccessible to bulk GaAs emitting at 300 K. At the wavelength corresponding to the bandgap of the GaAs host material, no luminescence signal is detected from the LED. This result demonstrates the SL character of the active region of the LED. The FWHM value of the electroluminescence spectrum is 60 meV, what is most likely to be due to size fluctuations of the V-shaped potential wells in the SL structure. The luminescence peak energy does not depend on the injection current over four orders of magnitude [6].

For the described LED structures also laser action has been demonstrated, at wavelength of 905 nm, and threshold current density of 2.2 kA/cm$^2$ [5].

## 2.2. Superlattice intersubband transition AlGaAs-GaAs far infrared LED

Several research groups have reported recently studies on intersubband transitions in superlattices and quantum wells. Applications ranging from logic devices and light modulators to infrared detectors have been considered [7]. Theoretical studies of the physical process and device applications have been undertaken, too.

In Ref. [7] a special SL structure which gives several improvements of the photoemission process has been considered on example of the AlGaAs-GaAs material system.

The device structure shown in Fig. 3 is a finite superlattice consisting of alternating narrow and wide wells separated by barriers. The narrow well is designed to have only one quasi-bound state $E_0'$, while the wide well has two states ($E_0$ and $E_1$). Under zero bias (upper part of Fig. 3), one has $E_0' = (E_0 + E_1)/2$ by adjusting the well width, w' and w. When biased to the operating point (lower part in Fig. 3), electrons are injected into the higher state of the wide well ($E_1$) via resonant tunneling through $E_0'$, and hence, the injection process is efficient (i.e., the tunneling probability is close to one). An electron in the higher state ($E_1$) can emit a photon (hν), and relax to the lower state ($E_0$). The relaxed electron continues to tunnel resonantly to the next wide well, and emits another photon, and so on.

The process described above could result in an amplification of the IR radiation, and hence, in an IR emitting device. The barrier widths are adjusted to be thin enough, so that the tunneling time through a double-barrier structure between two adjacent wide wells is somewhat faster than the radiative relaxation time. Compared to the simple SL structures, the present device offers efficient and rapid electron transfers between active regions (i.e., wide wells) and hence, favors the radiative emission processes. This scheme also offers the possibility of obtaining a population inversion between the higher and the lower states (laser action could be possible).

The described device structure is still under laboratory investigation, however, the data presented in Ref. [7] are sufficient to suggest interesting application possibilities in optoelectronic systems.

## 2.3. Blue LED

Wide band gap II–VI semiconductor compounds are promising materials for blue LEDs and laser diodes. However, because of the difficulties in growing low-resistive $p$-type ZnSe and ZnS, there are only few reports on blue electroluminescence in $p$-$n$ junction LEDs (mainly for structures grown by metalorganic chemical vapor deposition) The only one wide band gap II–VI semiconductor compound which exhibits $p$-type electrical conductivity is ZnTe. Unfortunately, the band gap energy of 2.26 eV of this compound does not correspond to blue light but to green light. However, if one uses the superlattices quantum size effect (dependence of the position on the energy scale of the discrete energy levels in a quantum well on the width of the well), and the possibility of creating a doped compositional superlattice exhibiting $p$-type conductivity [2], then in principle it should be possible to construct a blue light emitting diode of

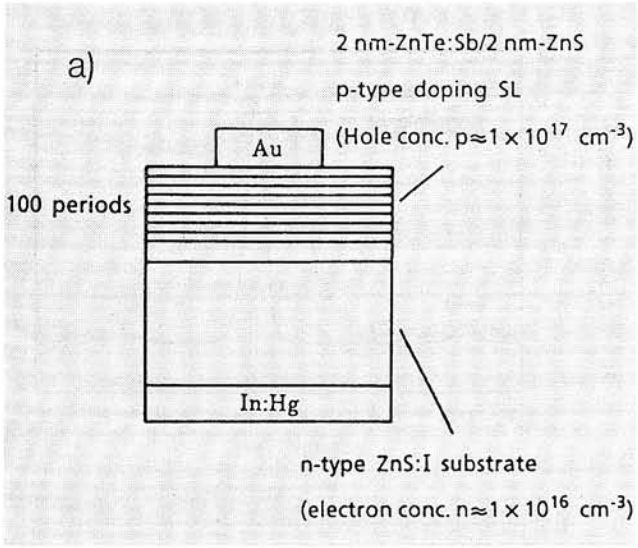


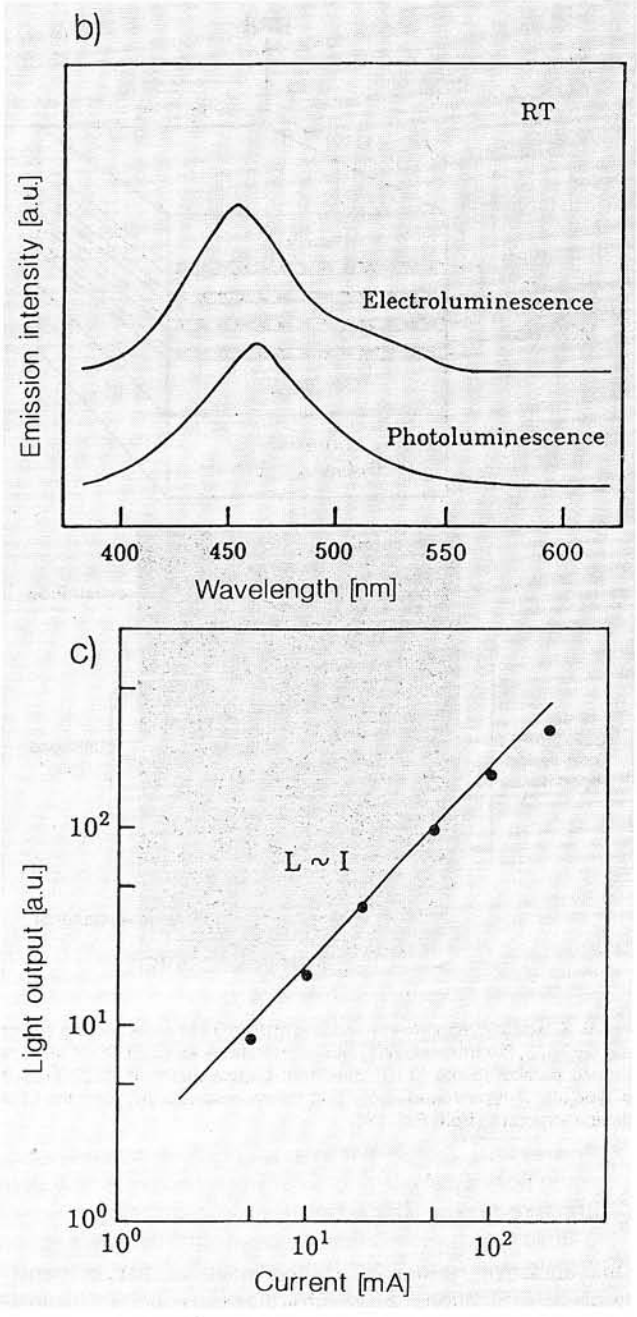


Fig. 4. a) The layer structure of the *p-n* junction LED with the p-ZnTe/ZnS doped compositional SL; b) EL and PL spectra measured at room temperature for the LED and SL structures,respectively; c) Total EL emission intensity of the LED at room temperature, as a function of the diode current (from Ref. [8])

*p-n* junction type in which the *p*-type side is created by a SL structure. A *p-n* junction blue LED using *p*-type ZnTe/ZnS SL structure has been demonstrated for the first time in Ref. [8].

Fig. 4a shows the layer sequence in the *p-n* junction diode. The device structure is composed of *p*-type doped compositional SL and *n*-type ZnS substrate. The *p*-type SL structure consists of 100 alternations of Sb-doped 2 nm ZnTe and undoped 2 nm ZnS. The electrode for the SL structure is an Au dot of 1mm diameter deposited onto the top SL layer by using a metal mask. The top layer of the SL is highly doped *p*-ZnTe. Ohmic contact to the back surface of the *n*-ZnS substrate is made of In:Hg alloy.

The electroluminescence spectra for the described structures of blue LEDs were investigated at room temperature. Fig. 4b shows the EL spectrum for the *p-n* diode and photoluminescence spectrum for the *p*-ZnTe:Sb/ZnS doped compositional SL. The forward bias voltage of the diode is 4V. The peak position of the EL well agrees with the photoluminescence (PL) peak position in the SL. The EL peak slightly shifts toward the higher energy side with increasing diode current, while the emission intensity increases linearly with the current (Fig. 4c).

## 2.4. Quantum wire LED

Strongly polarized PL and EL spectra have been obtained from strained $Ga_xIn_{1-x}P$ quantum wire (QWR) heterostructures grown on (100) oriented, on-axis GaAs substrates (Fig. 5a) by an *in situ* epitaxial technique [9]. The phenomenon of strain-induced lateral layer ordering (SILLO) has been exploited in order to create lateral superlattices [10] of $Ga_xIn_{1-x}P$ compositionally modulated in the [110] direction with a modulation period of 9.6 nm. The previous and subsequent growth of lattice-matched $Ga_{0.51}In_{0.49}P$ ternary alloy epilayers result in the formation of compressively strained QWRs. Transmission electron microscopy (TEM) shows (Fig. 5b) the wire cross sections to be about 4.8 x 20 nm. These structures exhibit 77 K PL spectra at 1.79 eV which are strongly (96%) polarized parallely to the wires (Fig. 6a) due to strain resulting from the lateral compositional modulation. The intensity of this emission depends critically on the polarization of the incident excitation. EL spectra from QWR LEDs display anisotropic polarization as well (Fig. 6b).

The heterostructure used in the QWR LED (Fig. 5a) has been grown by MBE [9]. The growth of a longitudinal $(GaP)_2/(InP)_2$ short-period superlattice (SPS) results in lateral superlattice formation via the SILLO process described in detail in Ref. [10]. The average In/Ga composition of the $(GaP)_2/(InP)_2$ SPS layer varies periodically along the [110] direction. Four of these nominally undoped, laterally ordered regions of about 20 nm thickness separated by 18 nm bulk lattice-matched $Ga_{0.51}In_{0.49}P$ barriers are imbedded between *p*-type and *n*-type $Ga_{0.51}In_{0.49}P$ above and below, respectively, forming a multiple QWR LED structure with the nominally undoped QWR array as the active region. A *p*-GaAs cap layer was included to form ohmic contact. The variation in the composition of the $Ga_xIn_{1-x}P$ in the laterally ordered region is determined from energy dispersive X-ray spectroscopy data to be at least $0.35 < x < 0.56$ [9].

In summary, it should be pointed out that the SILLO growth process is a consistent and reproducible method of multiple QWR LED fabrication. It could open a new doorway to novel electronic and optoelectronic device structures.

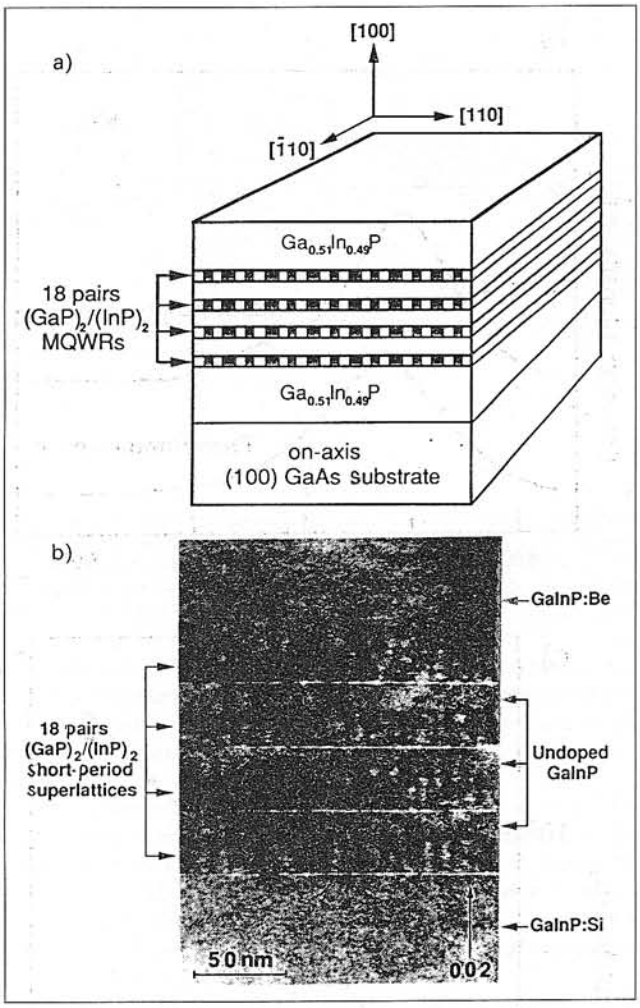


Fig. 5. Schematic diagram (a) and bright-field TEM cross section (b) of the $Ga_xIn_{1-x}P$ multiple QWR heterostructure. A strained QWR array is formed parallel to the [1̄10] direction. Lattice-matched $Ga_{0.51}In_{0.49}P$ $p$-type and $n$-type doped above and below, respectively, form the LED device structure (from Ref. [9])

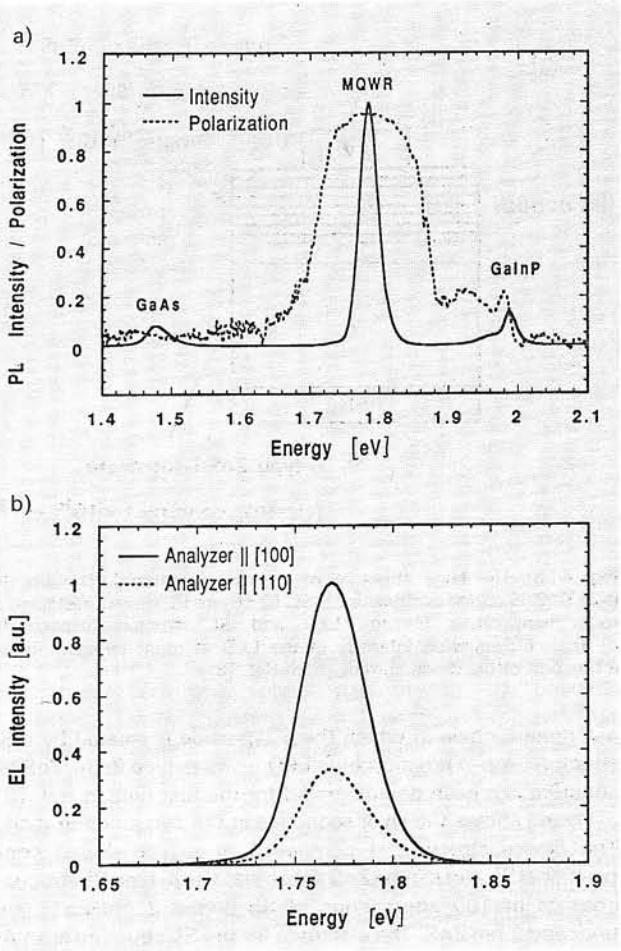


Fig. 6. a) The 77 K PL and PL polarization spectra of the multiple QWR heterostructure. The bulk $Ga_{0.51}In_{0.49}P$ and GaAs emission show little or no polarization, but the QWR luminescence polarization is 96%; b) The 77 K EL polarization spectra from the QWR LED emitting in the [1̄10] direction (see Fig. 5). The dominant polarization is in the [100] direction, perpendicular to the direction of the dominant strain (from Ref. [9])

## 3. Injection lasers

One attractive feature of a superlattice is that its density-of-states function $\rho(E)$, which is the most important parameter for determining the electronic and optical properties of semiconductor crystals, can be tailored by controlling the atomic arrangement of the constituent elements. For any bulk crystal or alloy, $\rho(E)$ is always parabolic with $\rho(E)=0$ at the bandedge. On the other hand, in superlattices the $\rho(E)$ is step-like with a finite value even at minimum energy [2]. This step-like density-of-states makes the SL structure superior in optical properties to bulk crystals [11]. Taking advantage of this, laser diodes with very low threshold have already been demonstrated long time ago [2]. In these diodes a MQW structure or a SL structure is usually adopted in the active region of otherwise standard double heterostructure (DH) lasers.

The MQW or SL segments which are anisotropic in structure cause advantageous device properties of the lasers [12]. Consideration of both the selection rule in the electron-to-hole recombination in this anisotropic structure, and of the energy separation between heavy and light holes in it, leads to the expectation that the optical gain for transverse electric (TE) polarized wave in the MQW waveguide would be much larger than that for transverse magnetic (TM) one. The experimental results of Ref. [11] demonstrate that the gain of the TE wave is larger by as much as 120 $cm^{-1}$ at the threshold than in the case of the TM wave, whereas the difference in a conventional DH structure is 20 $cm^{-1}$ at most. This large anisotropy in optical gain makes the laser with MQW or SL structures attractive as a polarization-stable optical source.

Since the first continuous wave DH GaAs/AlGaAs laser prepared by MBE the substantial progress has been made in reducing the current threshold and extending the lifetime [12]. To achieve low current threshold densities in structurally optimized DH lasers the high quality interfaces and the highest quality bulk crystal must be obtained. It has been pointed out that the bottom AlGaAs to GaAs active layer interface is inferior to the GaAs active layer to AlGaAs interface. This was attributed to the presence of interface roughness when GaAs is grown on top of AlGaAs [13]. During the course of studies on MQW lasers it became clear that the use of a few periods of superlattice at the heterointerface, just to smooth the interface, should help. This logic can be extended further and the average mole fraction of the superlattice can be graded down towards the GaAs layer.

With the graded SL structure current threshold densities as low as 600 $A/cm^2$ were obtained in DH lasers with a cavity length of about 300 $\mu$m and lasing at 880 nm. Without the SL interface structure the current threshold densities were considerably larger (1.2÷1.4 $kA/cm^2$) [14].

## 3.1 Quantum well lasers with superlattices

The original structure of graded index separate confinement heterostructure single quantum well (GRIN-SCH-SQW) lasers [12] undergoing continuous modifications at present, with the aim of improving both its crystalline structural perfection and its optical performance. The introduction of GaAs/AlGaAs (or GaAs/AlAs) SL structures in different parts of the laser structure has become a normal procedure in QW lasers technology. It has been shown that the introduction of a GaAs/AlAs SL buffer layer embedded at different depths between the GaAs substrate and the active layers clearly improves the device performance at the active region, in terms of lower threshold currents and higher quantum efficiency. All binary (AlAs)/(GaAs) short-period superlattices have been used to synthesize the cladding layer and optical cavity of a GRIN-SCH-SQW laser. These SL structures have also been used for the waveguide in the same type of laser diodes [15].

The origin of the improvements promoted by the introduction of the SL structures are linked to either a reduction of impurity flow coming from the thick AlGaAs layer growth front, or to a higher interface abruptness at the active region [2]. It has been shown [15] that radiative recombination in a SL-GRIN-SCH-SQW laser structure has strong excitonic origin, even at room temperature; a transition from bound exciton to free exciton emission takes place for temperatures above 100 K. Depending on the temperature, two regimes for the vertical transport through the SL structure to the laser QW have been discriminated. At low temperature, carrier transport is tunneling assisted, via localized states, and when a transparency temperature is reached, transport occurs via extended minibands. This transparency temperature depends on the SL composition and interface quality. The roughness of the thick ternary alloy underlaying the waveguide structure causes transparency to be reached at higher temperature, and this transparency is not total, as PL from the SL structure is observed even at room temperature. These results indicate that flatness of this bottom layer is mandatory to get the expected improvement by using SL structures to synthesize the waveguide material of a SCH-SQW laser [15]. An example of the layer sequence in GRIN-SCH-SQW laser structures is shown in Fig. 7.

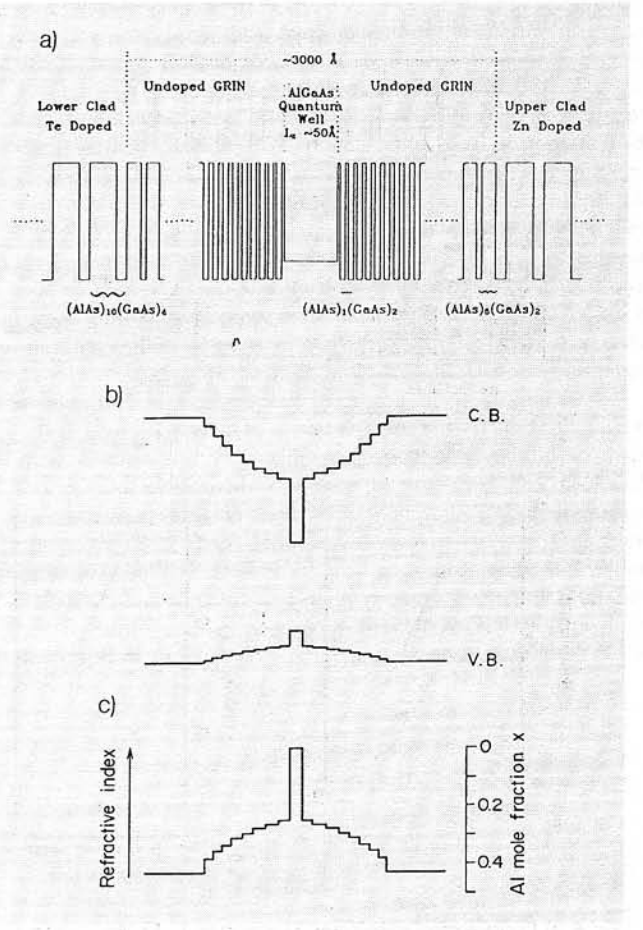


Fig. 7. a) The layer sequence in the SL-GRIN-SCH-SQW laser structure (the graded-index regions are produced by a linear variation in the AlAs barrier thickness, as shown); b) Schematic diagrams af the energy band structure; c) The refractive index profile of the laser structure with graded-layer-thickness superlattice waveguide (from Ref. [16] and [17], respectively)

## 3.2. Bragg reflectors for surface emitting laser diodes

Surface emitting optical devices with a vertical cavity have been investigated recently [18], for applications in optical interconnections. A vertical optical cavity consists of two distributed Bragg reflectors (DBRs) [12] or metallic mirrors at the top and the bottom of the device. The optical cavity structure allows optical multireflection, which achieves high efficiency for absorption type modulator and low threshold current for surface emitting laser diodes (SELD). Moreover, the vertical structure allows light emission and detection perpendicular to surfaces, thus enabling construction of small devices. These characteristics are advantageous for two-dimensional array integration.

Various devices have been investigated to take advantage of vertical cavities. For example, SELDs, detectors, modulators, SELDs integrated with heterojunction phototransistors, and optical functional devices such as vertical to surface transmission electrophotonic devices with a vertical cavity (VC-VSTEPs), have been reported [18].

The design of the DBRs, which form vertical cavities, determines many optical characteristics. In order to achieve low threshold current with SELDs, the reflectivity of these DBRs must be very high. Therefore, the two DBR materials need to have a large difference in the refractive indices. DBRs are often made with semiconductors to simplify the fabrication process. Semiconductor materials with large differences in refractive indices also have large band-gap differences. These band-gap differences cause high electrical resistance and excessing power consumption. The resistance can be reduced by several methods. One method is to inject current into the active layer from the side conductive layer bypassing the DBR mirrors. Another method is to form a thin layer of quasi-graded superlattice at the heterointerfaces in the DBR region. The latter method is aimed to reduce the potential barriers by the quasi-graded region at the heterointerfaces. This is effective in decreasing the DBR series resistance.

Fig. 8a shows the structure of the quasi-graded superlattices. Each interface has 9-pair SLs. The width of the AlAs SL layers ranges from 0.2 to 1.8 nm and the width of GaAs SL layers ranges from 1.8 to 0.2 nm. The total transition region length is 18 nm [18].

In order to investigate the effect of the quasi-graded SLs the series resistance of DBRs with an abrupt structure and with a quasi-graded structure have been compared. The investigated structures were as follows: a 0.4 $\mu$m thick $n$-GaAs and a 10-period AlAs/GaAs $n$-DBR mirror with abrupt (thickness of all SL layers is the same) or quasi-graded SLs were grown on an $n$-type GaAs substrate by using MBE. All epitaxial layers were Si doped at $2 \cdot 10^{18}$ cm$^{-3}$. The series resistance of the $p$-DBR mirrors was then examined as described in Ref. [18]. A 0.4 $\mu$m

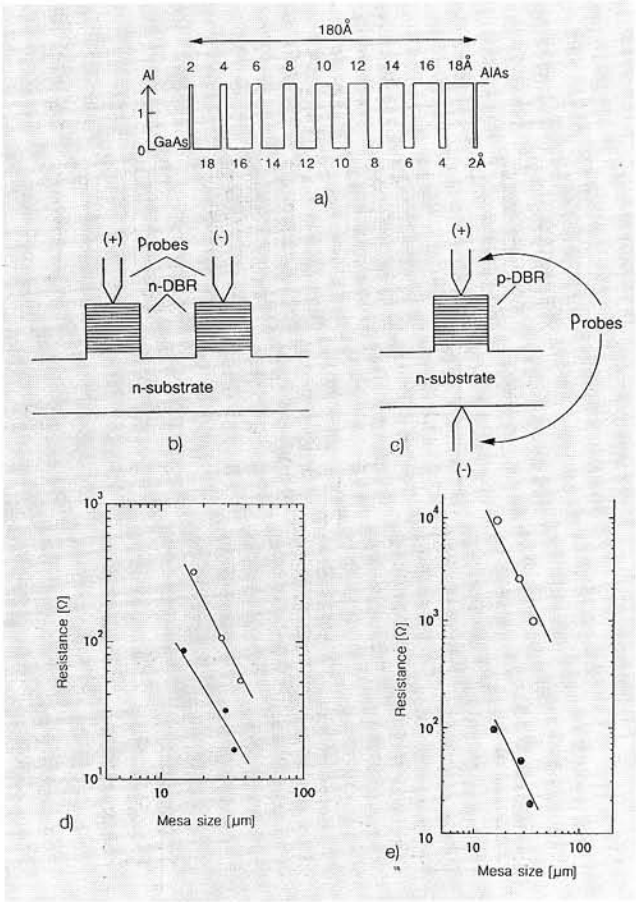


Fig. 8. a) Quasi-graded AlAs/GaAs SL structure; b) Experimental setup for measuring resistance of *n*-DBR; c) Experimental setup for measuring resistance of *p*-DBR; d) *n*-AlAs/GaAs DBR resistance as function of mesa size of the reflector; e) *p*-AlAs/GaAs DBR resistance as a function of the reflector mesa size. In (d) and (e) the circles show data for abrupt structure, while the dots show the data for quasi-graded structure (from Ref. [18])

thick *n*-type GaAs buffer layer, a 65 nm thick *p*-type GaAs buffer layer, and a 10-period AlAs/GaAs *p*-DBR mirror with abrupt or quasi-graded SLs were successively grown on a *n*-type GaAs substrate. The *p*-DBR mirrors were uniformly Be doped at $3 \cdot 10^{18}$ cm$^{-3}$. The cap ohmic contact layer was Be doped at $10^{19}$ cm$^{-3}$. These samples were fabricated into square elements by wet chemical etching. Alloyed electrodes were formed to lower contact resistance. AuZn alloyed contacts were used for the *p*-DBRs and AuGe/Ni alloyed contacts were used for the *n*-DBRs and the *n*-type substrates. The series resistances were measured at a fixed current density of 1.4 kA/cm$^2$.

The experimental results concerning the electric resistance of the SL DBR structures are shown in Figs. 8d and 8e. One may recognize from these results that a reduction in the series resistance of the DBR reflector may be reached by introducing quasi-graded SLs at the heterointerfaces. By using this SL structure one obtains the low series resistance of DBR reflector without compromising the high reflectivity. The mechanism of the reduction in the series resistance is based on an increase in tunneling current through the SL barrier layers [18].

### 3.3. Quantum wire laser structures

Quantum wire semiconductor lasers offer a number of advantages over standard quantum well lasers, including lower threshold current densities, increased modulation bandwidths, narrower spectral linewidths, and reduced temperature sensitivities [19]. The realization of the benefits described above have been demonstrated by applying the SILLO process, described in Sec. 2, to laser manufacturing [20].

The AlGaInP multiple QWR lasers were grown by a single-step gas source MBE [21], on (100)-oriented, on axis Si doped GaAs substrates. The schematic diagram of a typical laser diode is shown in Fig. 9a (compare it with the LED structure shown in Fig. 5). With this structure the first visible $Ga_xIn_{1-x}P/Al_{0.15}Ga_{0.35}In_{0.5}P$ multiple QWR laser diodes have been demonstrated [20]. Threshold current densities were greatly reduced for lasers fabricated with contact stripes in the [110] direction, perpendicular to the QWR array. Electroluminescence of these lasers (see Fig. 9b) is highly polarized and corresponds directly to the dominant strain present in the device structure. These multiple QWR laser diodes show great promise due to the high density of formed QWRs and their ease of fabrication.

Another possibility of growing with MBE QWR laser structures is based on tilted and serpentine SL structures (see the first part of the paper [6]). The schematic cross-section profile of the

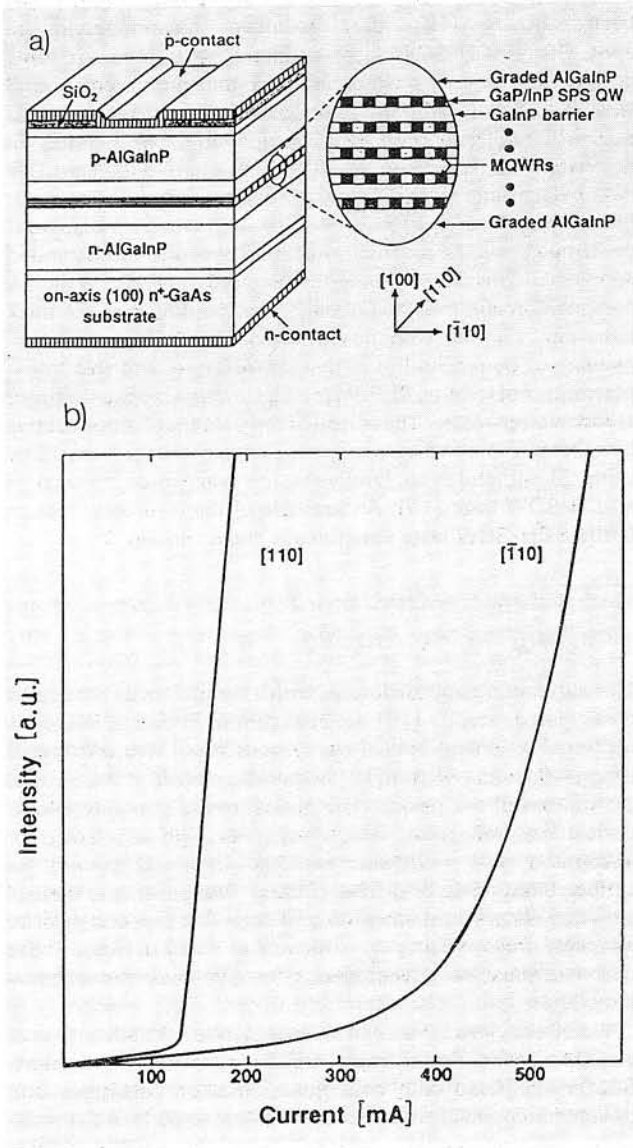


Fig. 9. a) Schematic illustration of a stripe geometry $Ga_xIn_{1-x}P/Al_{0.15}Ga_{0.35}In_{0.5}P$ GRIN-SCH multiple QWR laser grown on (100) on-axis GaAs substrate. The QWRs are alligned in the [1̄10] direction; b) Light output power vs pulsed injection current at 77 K for laser diodes shown in (a), with contact stripes aligned in the [1̄10] and [110] directions (from Ref. [20])

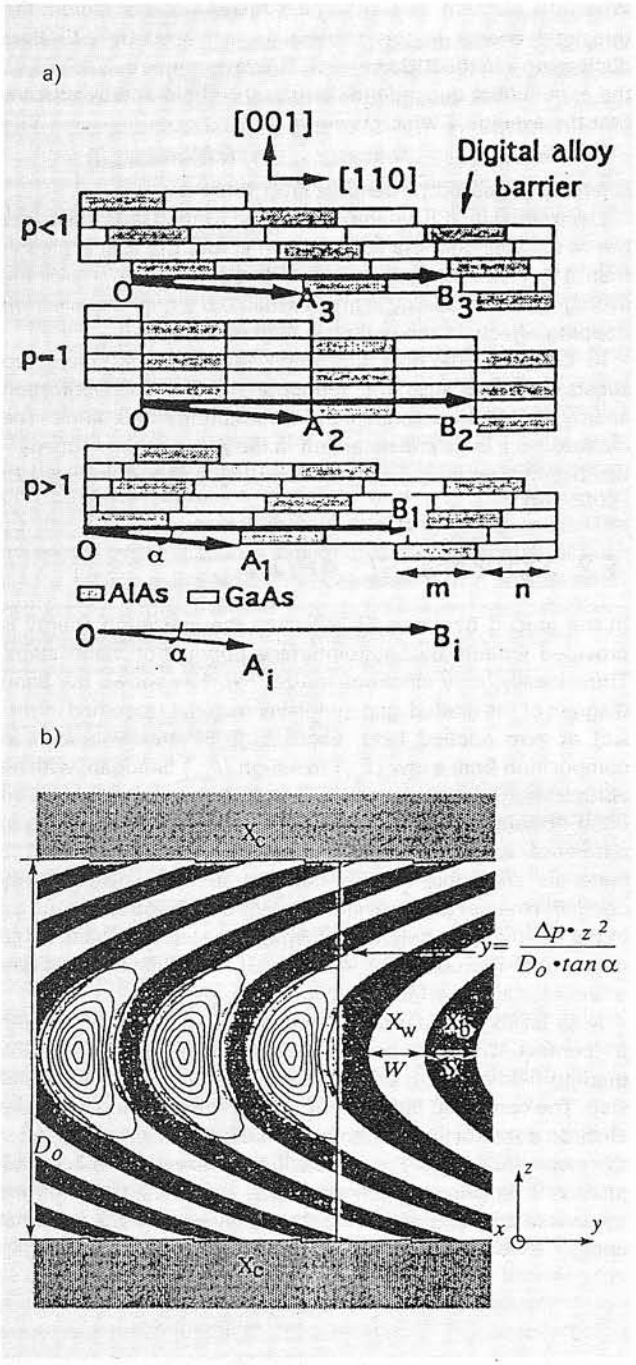


Fig. 10. a) Schematic cross-sectional profile of a SSL and its electron probability density for the lowest conduction band subband at zone center. The gray and white areas represent $Al_{0.5}Ga_{0.5}As$ and GaAs regions, respectively (from Ref. [22]); b) A SSL on terraced substrate depicted as three TSL slices (from Ref. [23])

SSL geometry is shown in Fig. 10. The curvature of the growth interface provides vertical confinement of the charge carriers in this structure. The degree of the confinement depends on the substrate tilt angle $\alpha$, the total thickness of the SSL $D_0$, and the intentional variation of the lateral growth rate $\Delta p$. The shape of the vertical curved interface can be expressed as $y=\Delta p z^2/(D_0 \tan\alpha)$. The tilt parameter $p$ is defined as $p=m+n$, where $m$ and $n$ are the fractions of barrier and well material on a step [6]. If the deposition or growth rate is adjusted such that $p=1$, then the amount of material deposited per monolayer exactly covers a step and the interface between the well and barrier material will grow vertically. If, however, $p<1$ or $p>1$ interface will tilt one way or the other (see Fig. 10b). The term $\Delta p=|p-1|$ indicates the intentional deviation from the nominal $p$ value of 1 and determines the slope of the interface.

It is obvious, that $\Delta p$, $\alpha$, and $D_0$ plus the Al contents in the wires, barriers and the claddings, respectively, are the parameters that are available to optimize the structure. The results of theoretical estimations concerning the optical gain characteristics of the SSL QWR laser are shown in Fig. 11. One may conclude that the considered laser structure, being still under laboratory investigation, is already promising and will probably become significantly improved in the nearest future, providing that good Al surface segregation will be done during the MBE growth.

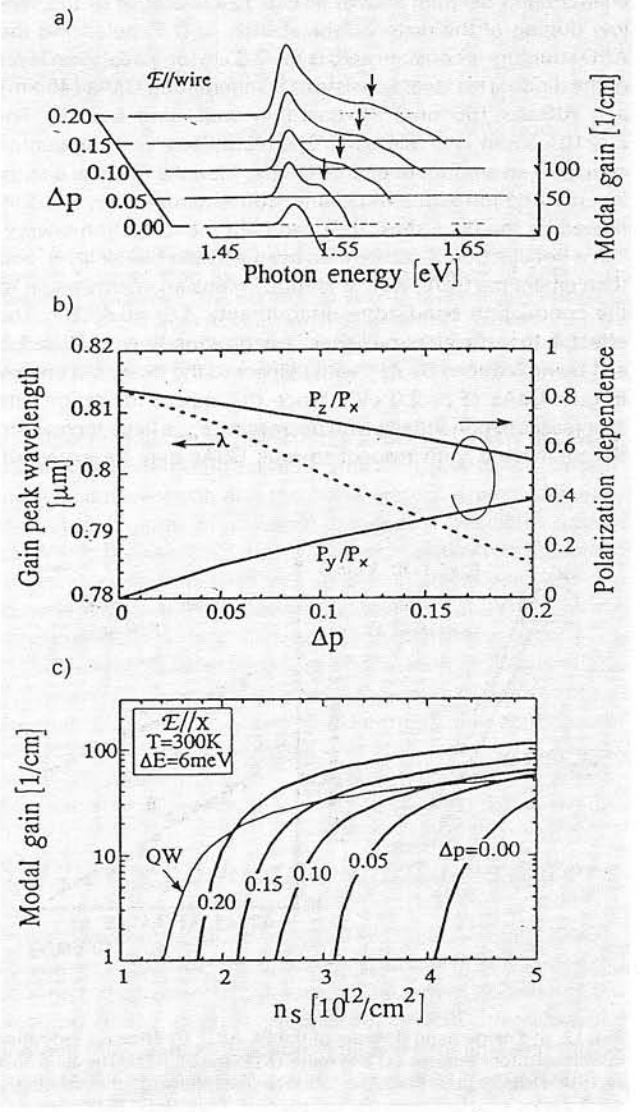


Fig. 11. Optical gain of a SSL with $x_b=x_c=0.5$, $W=S=5.4$ nm, $D_0=46$ nm, $T=300$ K, and width $\Delta E=6$ meV of the assumed Gaussian line shape function for modal gain: a) Modal gain spectrum at injected surface carrier density $n_s=5\cdot10^{12}$ cm$^{-2}$ with electric field $E$, polarized along the wire axis (arrows indicate the second gain peak); b) Gain peak wavelength and polarization dependence of the peak gain ($P_x$, $P_y$ and $P_z$ are the peak gains when the electric field is polarized in $x$, $y$, and $z$ directions, respectively); c) Maximum modal gain as a function of injected surface carrier density for different $\Delta p$ values. Electric field is polarized along the wire axis. QW is a 5.4 nm thick SQW of $GaAs/Al_{0.5}Ga_{0.5}As$ (from Ref. [22])

## 4. Avalanche photodiodes

A large ratio of the ionization coefficients $\alpha/\beta$ for electrons and holes is required to achieve low noise at high gain in avalanche photodiodes (APDs) [24]. These diodes are widely used in optical-fibre communication systems. The 0.8 $\mu$m wavelength fibre-optic systems use low-noise silicon APDs, which exhibit $\alpha/\beta \approx 50$. Modern systems, however, operate at longer wavelengths (typically 1.3 $\mu$m) to take advantage of lower fibre losses. III–V APDs are usually suggested for these systems. Unfortunately, $\alpha/\beta$ for most III–V compounds is approximately unity, resulting in increased avalanche multiplication noise. Thus, methods for increasing $\alpha/\beta$ in these materials are of considerable practical importance.

Three structures which enhance $\alpha/\beta$ ratio have been demonstrated in the early 80ties. These are the AlGaAs-GaAs superlattice APD [25], the staircase SL APD [26], and the channeling APD based on doped compositional SL or MQW structures [27]. All of the listed structures increase $\alpha/\beta$ in the bulk material to 5 or even to 10.

### 4.1. AlGaAs-GaAs SL APD

In the SL APD structure, enhancement of the $\alpha/\beta$ ratio is due to band-edge discontinuity assisted impact ionization (the conduction band discontinuity provides 25% of the electron ionization energy). To understand this let us consider the energy band diagram shown in Fig. 12a. Because of the very low doping of the material, the electric field $F_z$ polarizing the APD structure is constant across the 2.5 $\mu$m long depletion layer of the diode. This layer consists of 50 alternating GaAs (45 nm) and AlGaAs (55 nm) SL quantum wells and barriers. For $F_z > 10^5$ V/cm, the electrons gain between two sequential collisions an amount of energy greater than the average energy lost per phonon scattering event. Consequently, they become heated by the field, thus, they can gain the ionization energy.

If a hot electron is accelerated in an AlGaAs barrier layer, and then enters the GaAs well, it abruptly gains an energy equal to the conduction band-edge discontinuity $\Delta E_C = 0.48$ eV. The effect is that the electron "sees" a ionization energy ($E_{th} \approx 1.5$ eV) being reduced by $\Delta E_C$ with respect to the threshold energy in bulk GaAs ($E_{th} = 2.0$ eV). Since the impact ionization rate $\alpha$ increases exponentially with decreasing $E_{th}$, a large increase in the effective $\alpha$ with respect to bulk GaAs may be expected.

When the electron enters the next AlGaAs barrier region, the threshold energy in this material is increased by $\Delta E_C$ thus decreasing $\alpha$ in the AlGaAs layer. However, since $\alpha_{GaAs} \gg \alpha_{AlGaAs}$, the exponential dependence on the threshold energy ensures that the average $\alpha$ which is equal to

$$\alpha = (\alpha_{GaAs} L_{GaAs} + \alpha_{AlGaAs} L_{AlGaAs}) / (L_{GaAs} + L_{AlGaAs})$$

is largely increased ($L$ denotes layer thicknesses).

Electrons which have impact ionized in the GaAs easily get out of the well, and the voltage drop across the well is greater than 1V. Additionally, at fields $F_z > 10^5$ V/cm in GaAs the average electron energy is greater than 0.6 eV, so that electron trapping effects in the wells are negligible.

In contrast, the hole ionization rate $\beta$ is not increased substantially because the reduction in the hole ionization energy is only the valence band discontinuity of 0.08 eV. The net result is a large enhancement in the $\alpha/\beta$ ratio. The superlattice detector wafer grown by MBE [25] is shown in Fig. 12b (the inset).

### 4.2. Staircase SL APD

In the graded-bandgap SL structure the ionization energy is provided entirely by heterointerface conduction band steps. Thus, ideally, only electrons ionize. Fig. 13a shows the band diagram of the graded-gap multilayer material (assumed intrinsic) at zero applied field. Each stage is linearly graded in composition from a low ($E_{g1}$) to a high ($E_{g2}$) bandgap, with an abrupt step back to low-bandgap material. The conduction band discontinuity shown accounts for most of the bandgap difference, what is typical of many III–V heterojunctions. The materials are chosen for a conduction band discontinuity comparable to or greater than the electron ionization energy $E_{ie}$ in the narrow-gap material following the step. The band-edge diagram of the complete staircase SL APD device structure under bias is shown in Fig. 13b.

Now let us consider a photoelectron generated next to the $p^+$ contact. Under the combination of the bias field $F_z$ and the grading field $\Delta E_C/l$, it drifts toward the first conduction band step. The combined field $F_z - \Delta E_C/l$ is small enough so that the electron does not impact-ionize before it reaches the step. After the step, since $\Delta E_C \approx E_{ie}$, the electron ionizes by impact. This process is repeated in each stage after each step, the electrons transverse a graded region in which they acquire the potential energy used for impact ionization in the narrow-bandgap

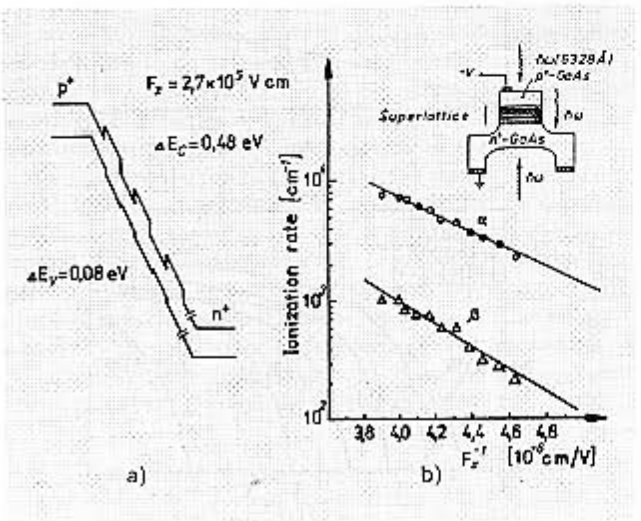


Fig. 12. a) Energy band diagram of the SL APD; b) Effective ionization coefficients for electrons ($\alpha$) and holes ($\beta$) in the SL APD. The solid lines represent least-square fits to the data. The inset shows a schematic of the APD device structure with the superlattice (from Ref. [25])

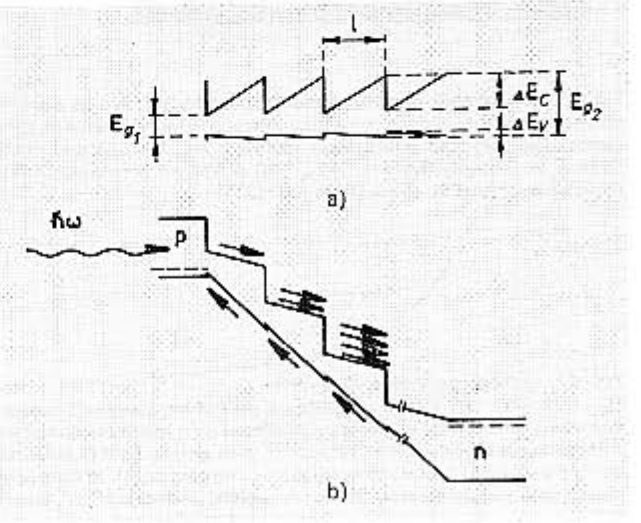


Fig. 13. a) Band diagrams of the unbiased graded multilayer region; b) The complete device structure of the staircase SL APD under bias (from Ref. [26])

region following the next interface. Ideally, the avalanche gain per stage is exactly 2. Each electron impact ionize once after each conduction band step. In fact, the gain is $2-\delta$, where $\delta$ is the fraction of electrons which do not impact-ionize. The total gain of the structure is then equal to $M=(2-\delta)^N$, where $N$ is the number of stages. Most of the electrons impact-ionize if their energy is a tenth of an eV or so above the ionization energy $E_{ie}$. The competing loss mechanism is optical phonon emission. The high ionization probability is caused by the quadratic increase of the ionization cross-section above $E_{ie}$ as a result of the density of states and because several phonons must be emitted to reduce the electron energy below $E_{ie}$.

Any hole ionization is caused only by the applied electric field $F_z$. The valence band steps are of the wrong sign to assist ionization. For electron transport across the graded region this bias field $F_z$ must cancel the $\Delta E_C/l$ conduction band quasi-electric field and provide a small extra component to assure drift, rather than diffusion transport. The device is then designed so that the hole ionization rate at $F_z > \Delta E_C/l$ is small. The maximum multiplication is determined by the number of such stages, which is limited by the depletion width at the lowest achievable intrinsic-region doping. Because only electrons cause ionization, this device mimics a photomultiplier. The conduction band steps correspond to dynodes [28].

## 4.3. Channeling APD

Fig. 14a shows a schematic diagram of the channeling APD structure. This consists of several abrupt $p$-$n$ heterojunctions with alternated $p$ and $n$ layers of bandgap $E_{g1}$ and $E_{g2}$ ($E_{g1} > E_{g2}$), respectively. The layers, lattice-matched to a semi-insulating substrate, may create a MQW structure, with high confinement of charge carriers [27], or can be grown as a doped compositional SL structures with only weak or no carriers confinement [28]. The $p^+$ and $n^+$ regions, which extend perpendicular to the layers, can easily be obtained by ion implantation. The voltage source supplying the reverse bias is connected between the $p^+$ and the $n^+$ region. Equal doping levels ($n=p=N$) for the $n$ and $p$ layers are required.

For zero bias the $p$ and $n$ layers are in general only partially depleted on both sides of the heterojunction interfaces. The undepleted portions of the $p$ and $n$ layers are at the same potential of the $p^+$ and $n^+$ end regions, respectively, so that the structure appears as a single interdigitated $p$-$n$ junction. Because of this geometry, when a reverse bias is applied between the $p^+$ and $n^+$ regions, this potential difference will appear across every $p$-$n$ heterojunction, thus increasing the space-charge width on both sides of the heterojunction interfaces until all the $p$ and $n$ layers are completely depleted. At this point, analogously to a $p^+$-$i$-$n^+$ diode, any further increase in the reverse bias will only add a constant electric field parallel to the length $L$ of the layers. This field ($\varepsilon$ in Fig. 14b) is then increased to values such that avalanche multiplication takes place.

Fig. 14b is a 3-dimensional picture of the APD band structure under operating conditions. Suppose that radiation of suitable wavelength is absorbed in the narrow-gap layers, thus creating electron-hole pairs. The two $p$-$n$ heterojunctions formed at the heterointerfaces between the relatively narrow bandgap and the surrounding higher bandgap layers serve to confine electrons to the narrow bandgap layers while sweeping holes out into the contiguous wider bandgap $p$-layers where they are confined by the potential. The parallel electric field $\varepsilon$ causes electrons confined to the narrow bandgap layers to impact ionize. Holes generated this way are swept out in the surrounding higher-gap layers before undergoing ionizing collisions in the narrower gap layers since the layer thickness is made much smaller than the hole ionization distance $1/\beta$. Conversely, electrons generated

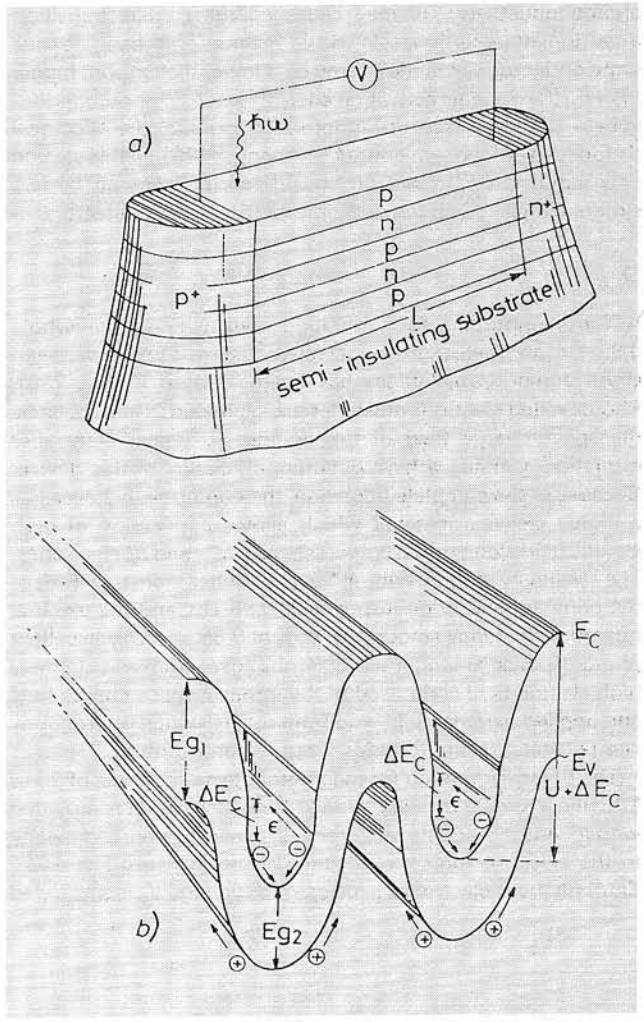


Fig. 14. a) Schematic diagram of APD (not to scale). The $p$ layers have a wider bandgap than the $n$ layers; b) Band diagram of APD under operating conditions. The $\varepsilon$ is parallel electric field causing carriers to ionise. $U+\Delta E_c$ is the electron confining potential. The valence band discontinuity has been assumed negligible with respect to $\Delta E_c$. The electron-hole separation mechanism is also shown (from Ref. [27])

by impact ionisation of holes in the wider gap layers are swept out before undergoing multiplication in these layers. In conclusion, the electrons and the holes impact ionise in spatially separated regions of different bandgap. The holes in the wider-gap layers impact ionise at a much smaller rate compared to the electron ionisation rate in the relatively narrower-gap material, due to the exponential dependence of $\alpha$ and $\beta$ on the bandgap, so that $\alpha/\beta$ can be made extremely large [27].

Theoretical studies based on many-particle Monte-Carlo technique [28] have evidenced that the optimal performance of the channeling APD is not achieved through high confinement of electrons in the GaAs layers and holes within the AlGaAs (a MQW structure variant), but rather through weak confinement (the SL structure variant) in the APD active region.

# 5. Photoconductive photodetectors

A photoconductive photodetector (PPD) is essentially a radiation sensitive resistor. The operation principle of a PPD is based on direct absorption of photons in the active material of the detector. In the case of semiconductor PPD the absorbed photons may produce electron-hole pairs (band-band transitions) in the semiconductor when the energy $h\nu$ of photons is greater than, or equal to the bandgap energy $E_g$ (intrinsic

photoconductivity), or may cause charge carriers transition from dopants energy levels to the main energy-bands of the semiconductor, when the energy $h\nu$ is lower than $E_g$, but higher than $E_a$, the dopants activation energy (extrinsic photoconductivity). In both cases of photon absorption the electrical conductivity of the semiconductor changes [29]. In this section only extrinsic PPDs will be considered, because so far, SL structures have been applied only to these photodetectors.

## 5.1. PPDs based on doping SLs

A GaAs photodetector with high sensitivity in the whole $0.8 \div 1.4$ $\mu$m wavelength range, fabricated from totally depleted GaAs doping superlattices has been reported in Ref. [30]. Photoexcited electrons and holes are separated in real space by the space-charge field of the doping SL immediately after excitation, yielding a high quantum efficiency of this device. Because of the complete depletion, the doping SL behaves like a highly resistive material which allows application of high electric field along the layers via selective $n^+$- and $p^+$ electrodes. The sensitivity of this device at 1.3 $\mu$m reaches more than 90% of the original band-edge response at 0.85 $\mu$m, and the external quantum efficiency amounts to 65% at 0.85 $\mu$m. This excellent photoresponse at longer wavelengths arises from an extremely high electric field composed of the intrinsic space charge field and applied external field, and from the existence of pronounced tail states in the forbidden gap region of the SL.

The SL configuration for the photodetector consists of 20 to 100 thin alternate $n$- and $p$-doped GaAs layers and is provided with $n^+$ and $p^+$ regions on the edges extending perpendicularly to the layers to form the selective electrodes (see Fig. 15a). Through these electrodes a reverse bias voltage $V_R$ is applied to all constituent $p$-$n$ junctions of the SL. Operation of the detector can be understood by inspection of Fig. 15. The periodic modulation of the energy bands by the positive and negative space charge in the respective layers is indicated in Fig. 15b. A SL configuration has been chosen where the constituent layers are already totally depleted at zero bias. This requires design parameters providing equal doping densities, i.e., $N_D d_n = N_A d_p$, and an effective gap of $0 < E_{g,eff} < E_g$. In this structure the intrinsic space-charge field $F_0(x)$ given by the design parameters remain constant upon variation of the reverse bias, because the donors and the acceptors within the respective layers are already completely ionised at zero bias.

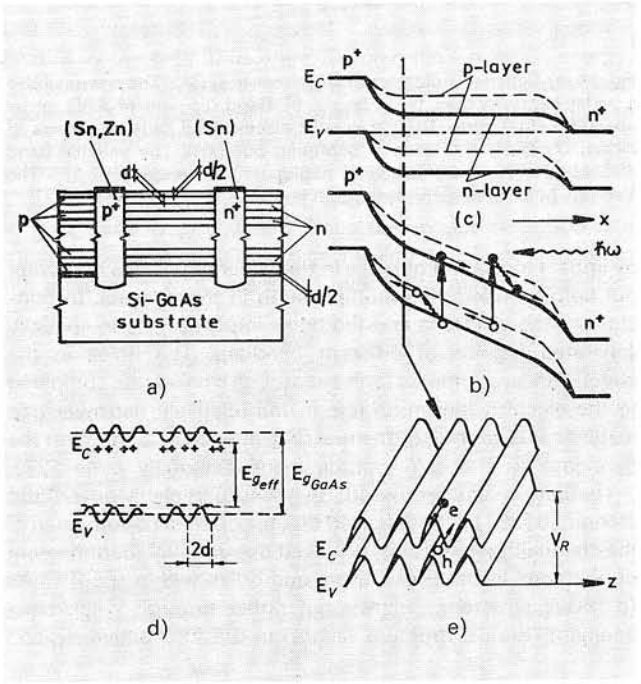


Fig. 15. a) Layer sequence of GaAs doping SL and arrangement of selective $n^+$- and $p^+$-electrodes; b) Periodic modulation of real-space energy bands by the positive and negative space charge in the respective layers; c) Schematic real-space energy band diagram of a semi-insulating GaAs doping SL at zero bias in $x$-direction along the layers viewing the centre of each layer type; d) The SL under operating conditions at high reverse bias with the longitudinal external field tilting the whole structure; e) Vertical section showing the periodic modulation of tye energy bands in $z$-direction and indicating the sweep-out of electrons and holes along the parabolic well channels in the tilted structure (from Ref. [30])

Under these conditions the conduction and valence band-edges are flat along the layers, i.e., in the $x$ direction, as shown in Fig. 15c, except for the area close to the $n^+$ and $p^+$ contact regions. Because of the total depletion of the layers, the SL is highly resistive and behaves like a semi-insulator. Therefore, when a reverse bias is applied via the selective electrodes, a constant longitudinal electric field $F_l$ is added in $x$ direction parallel to the length of the layers, i.e., the structure is tilted in layer direction, as indicated in Figs. 15d and 15e. Electron-hole pairs generated by absorption of light are effectively separated in $z$ direction by strong space-charge field of the SL and then immediately swept away by the longitudinal field in $x$ direction to the respective electrodes. As a result, recombination of photogenerated carriers is negligibly small and extremely high efficiencies of the absorption process are achieved.

Since the photogenerated carriers have relaxation times as short as 1 ps for thermalization in the conduction and valence subband systems the device speed is determined mainly by the time required to sweep out the confined electrons and holes along the parabolic well channels. In addition, due to the rapid sweep-out of the photogenerated carriers by the longitudinal electric field at high reverse bias, the bare space-charge potential of the superlattice experiences only a minor compensation from these excess carriers, and the responsivity of the device for long-wavelength irradiations does not deteriorate during its operation.

## 5.2. HgTe/CdTe SL PPD

The HgTe/CdTe superlattice was originally proposed as an IR material in 1979 [31]. It was shown that the band gap of the SL structure could be controlled by selecting the SL layer thicknesses and that most of the useful regions of the IR spectrum could be sampled. Changing the HgTe layer thickness in the SL structure from 3.5 nm to 11 nm one may change the cutoff wavelength of the detector ($\lambda_c = hc/E_g^{SL}$) from 5 to 14 $\mu$m, respectively (see Fig. 16).

It was predicted that a precise control of the thickness of SL layers were required. The best suited growth technique for HgTe/CdTe SL structures is MBE [33], because (i) growth temperature is low and, therefore, serious interdiffusion is avoided; this fact ensures the required abruptness of heterointerfaces in the superlattice; and (ii) MBE grown HgTe and CdTe layers of the SL structure possess sufficiently high structural perfection and may still be improved.

All of the studies concerning the HgTe/CdTe SLs, which have been cited above were based on the assumption of a small valence-band offset, $\Delta E_V \leqslant 40$ meV in these structures. However, it is recognized now that numerous aspects of the SL properties can be understood only in terms of a large $\Delta E_V$, the most frequently employed value being 350 meV [34]. The recent fabrication by MBE of a high quantum efficiency SL detector operating at 5 $\mu$m [35] makes it particularly worthwhile to reassess the earlier predictions of detector properties of HgTe/CdTe SLs.

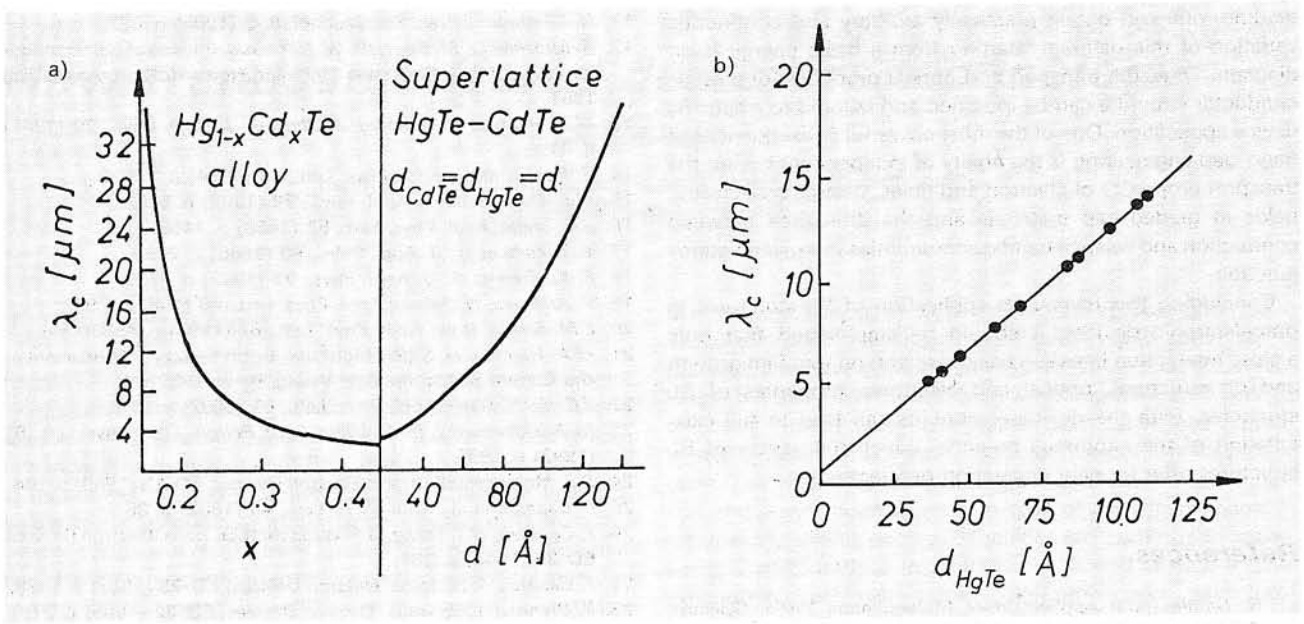


Fig. 16. a) Cutoff wavelength as a function of alloy composition (left panel) for the $Hg_{1-x}Cd_xTe$ alloy and as a function of layer thickness (right panel) for HgTe/CdTe superlattice with equally thick HgTe and CdTe layers (from Ref. [31]); b) The room temperature cutoff wavelength of HgTe/CdTe SLs with $d_{CdTe} \leqslant 3.5$ nm as a function of the HgTe layer thickness. The experimental data are given by the circles and the solid line is the linear fit (from Ref. [32])

It is shown in Fig. 17 a calculated SL cut-off wavelengths as a function of HgTe well thickness $d_W$ for a typical detector operating temperature of 77 K. The barrier thickness $d_B$ is held constant at 5 nm and there are given the results for both the [100] (dashed) and [211] (solid) orientations of the SL growth. It is also shown for comparison purposes the early results of Smith et al. [31] for $d_B = d_W$, who assumed a valence-band offset of zero. It is evident that this and other earlier estimates of the appropriate well thicknesses for long wavelength IR detectors must be revised considerably. This remark concerns other detector parameters as well. For example, Fig. 17b shows the cutoff wavelength fluctuations $\Delta\lambda_c$ versus $\lambda_c$, which are due to variation in the growth parameters of the SL structure, namely, the effusion cell temperatures.

It can be concluded that the cutoff wavelength is still more easily controlled in the HgTe/CdTe SL than in the $Hg_{1-x}Cd_xTe$ alloy, although the improvement one gains in the device parameters by using SL structures is smaller than originally predicted using $\Delta E_V = 0$ for the heterointerfaces in the HgTe/CdTe SL structures [34].

## 6. Outlook

The advent of MBE [20] enables the development of a new class of materials and heterojunctions with unique electronic and optical properties. Most noticable among these are: (i) compositional and doping SLs, (ii) doped compositional SLs, (iii) strained layer SLs, and (iv) variable-gap SLs. The investigation of the novel physical phenomena possible by means of such structures has proceeded parallel with their exploitation in novel devices. As a result a new approach to design of heterojunction semiconductor devices, called band-gap engineering, has gradually emerged [36].

The starting point of band-gap engineering is the realization of the extremely large number of combinations which are possible in the SLs and heterojunction structures mentioned above. This allows designing of a large variety of new energy band diagrams. Particularly, through the use of band-gap

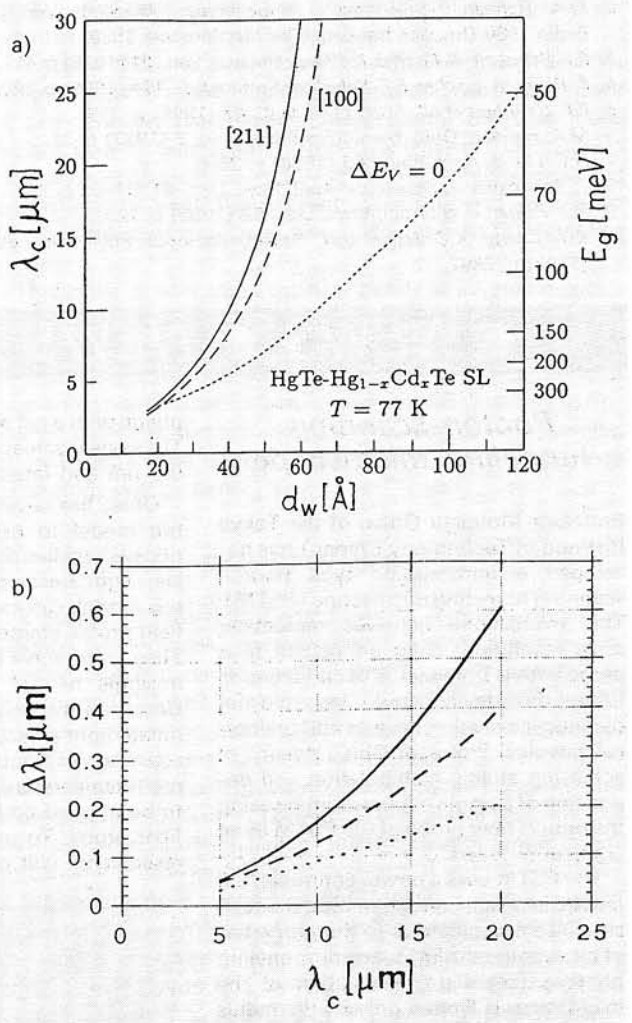


Fig. 17. a) Cutoff wavelenght and energy gap vs well thickness for [100] and [211] superlattices with $d_B = 5$ nm at 77 K. The dotted curve ($d_B = d_W$) represents the early calculations of Smith et al. [31], based on the assumption of zero valence-band offset (see Fig. 16a, left panel); b) Calculated cutoff wavelength fluctuations vs cutoff wavelength, due to variations in the MBE Hg-effusion cell temperatures. Results are shown for the $Hg_{1-x}Cd_xTe$ alloy (solid curve), and for HgTe/CdTe SLs with valence-band offsets of 0 (dotted curve) and 350 meV (dashed curve) (from Ref. [34])

grading, one can obtain practically arbitrary and continuous variation of this diagram, starting from a basic energy band diagram. Thus, the transport and optical properties of a semiconductor structure can be modified and tailored to a specific device application. One of the most powerful consequences of band-gap engineering is the ability of independent tuning the transport properties of electron and holes, using quasi-electric fields in graded-gap materials and the difference between conduction and valence band discontinuities in a given heterojunction.

Concluding this review on application of SL structures in optoelectronic devices, it should be emphasized that only a close interaction between basic research on thin film growth and on structural, optical and electronic properties of SL structures, with the device electronics can lead to full exploitation of the enormous potential which the variety of SL structures offer for new generation optoelectronics.

## References


1. *R. Dingle* (ed.): Application of Multiquantum Wells, Selective Doping, and Superlattices. Semiconductors and Semimetals, Vol. 24, Academic Press, Boston 1987.
2. *M.A. Herman:* Semiconductor Superlattices. Akademie Verlag, Berlin 1986 (Russian translation by Mir, Moscow 1989).
3. *E.F. Schubert, A. Fischer, K. Ploog:* Electron. Lett., **21** (1985) p. 411.
4. *K. Ploog, A. Fischer, E.F. Schubert:* Surface Sci., **174** (1986) p. 120.
5. *E.F. Schubert et al.:* Appl. Phys. Lett., **47** (1985) p. 219.
6. *M.A. Herman:* Opto-Electronics Review, no. **2** (1993) p. 31.
7. *H.C. Liu:* J. Appl. Phys., **63** (1988) p. 2856.
8. *T. Yokogawa, T. Narusawa:* Appl. Phys. Lett., **61** (1992) p. 291.
9. *P.J. Pearah* et al.: Appl. Phys. Lett., **62** (1993) p. 729.
10. *K.Y. Cheng, K.C. Hsieh, J.N. Baillargeon:* Appl. Phys. Lett., **60** (1992) p. 2892.
11. *H. Okamoto:* J. Vac. Sci. Technol. B, **3** (1985) p. 687.
12. *B. Mroziewicz, M. Bugajski, W. Nakwaski:* Physics of Semiconductor Lasers. PWN, Warszawa 1991 and North-Holland, Amsterdam 1991.
13. *M.A. Herman, D. Bimberg, J. Christen:* J. Appl. Phys., **70** (1991) p. R1.
14. *R. Fischer* et al.: Appl. Phys. Lett., **44** (1984) p. 1.
15. *M.L. Dotor* et al.: J. Appl. Phys., **72** (1992) p. 5861.
16. *J.R. Sheal:* Appl. Phys. Lett., **52** (1988) p. 1455.
17. *Y. Tokuda* et al.: J. Appl. Phys., **60** (1986) p. 2729.
18. *K. Kurihara* et al.: J. Appl. Phys., **73** (1993) p. 21.
19. *Y. Arakawa, H. Sakaki:* Appl. Phys. Lett., **40** (1982) p. 939.
20. *E.M. Stellini* et al.: Appl. Phys. Lett., **62** (1993) p. 4588.
21. *M.A. Herman, H. Sitter:* Molecular Beam Epitaxy – Fundamentals and Current Status, Springer Verlag, Berlin 1989.
22. *J.C. Yi, N. Dagli:* Appl. Phys. Lett., **61** (1992) p. 219.
23. *M. Krishnamurthy, M.-S. Miller, P. M. Petroff:* Appl. Phys. Lett., **61** (1992) p. 2990.
24. *R.J. McIntyre:* IEEE Trans. Electron Devices, **ED-13** (1960) p. 164.
25. *F. Capasso* et al.: Appl. Phys. Lett., **40** (1982) p. 38.
26. *F. Capasso, W.T. Tsang, G.F. Williams:* IEEE Trans. Electron Devices, **ED-30** (1982) p. 381.
27. *F. Capasso:* IEEE Trans. Electron Devices, **ED-29** (1982) p. 1388.
28. *K. Brennan:* IEEE Trans. Electron Devices, **ED-32** (1985) p. 2197; and p. 2467.
29. *A. Rogalski, J. Piotrowski:* Progress in Quantum Electronics, **12** (1988) p. 87.
30. *Y. Horikoshi, K. Ploog:* Appl. Phys. A, **37** (1982) p. 47.
31. *D.L. Smith, T.C. McGill, J.N. Schulman:* Appl. Phys. Lett., **43** (1983) p. 180.
32. *J. Reno* et al.: J. Vac. Sci. Technol. A, **5** (1987) p. 3107.
33. *M.A. Herman, M. Pessa:* J. Appl. Phys., **57** (1985) p. 2671.
34. *T.H. Myers* et al.: Appl. Phys. Lett., **61** (1992) p. 1814.
35. *K.A. Harris* et al.: J. Vac. Sci. Technol. B, **9** (1991) p. 1752.
36. *F. Capasso*: in: Heterojunction Band Discontinuities: Physics and Device Applications (*F. Capasso* and *G. Margaritondo* – eds.). Elsevier Sci. Publ., Amsterdam 1987, p. 399.